

A Comparison of Initial Developments Between Explosive and Ordinary Mid-latitude Cyclones Off the East Asian Coast in Winter

Xiaoyu Gao (✉ 954851432@qq.com)

Tsinghua University Department of Earth Sciences <https://orcid.org/0000-0001-9078-3843>

Ping Lu

Tsinghua University Department of Earth Sciences

Yang Hu

Tsinghua University Department of Earth Sciences

Shuqin Zhang

Tsinghua University Department of Earth Sciences

Xiaoyan Sun

Tsinghua University Department of Earth Sciences

Qiuyang Zhang

Tsinghua University Department of Earth Sciences

Research Article

Keywords: Explosive cyclones (ECs), Weather Research and Forecast (WRF), diabatic processes, PV

Posted Date: December 3rd, 2021

DOI: <https://doi.org/10.21203/rs.3.rs-890124/v1>

License: © ⓘ This work is licensed under a Creative Commons Attribution 4.0 International License.

[Read Full License](#)

A comparison of initial developments between explosive and ordinary mid-latitude cyclones off the East Asian coast in winter

Xiaoyu Gao^{1,2} · Ping Lu² · Yang Hu² · Shuqin Zhang³ · Xiaoyan Sun⁴ · Qiuyang ZHANG⁵

Abstract

Explosive cyclones (ECs) off the East Asian coast pose challenges in forecasting and significant threats to human life and property. In searching for the key features that distinguish explosive cyclones (ECs) from ordinary extratropical cyclones (OCs), this study presents detailed comparison of winter ECs versus OCs in the perspective of potential vorticity (PV) using 10 years of reanalysis data with high temporal and spatial resolutions. ECs feature greater low-level baroclinity and stronger PV than OCs. The decomposition of local PV tendency shows the important contribution of cold advection (with correlation coefficient of 0.8) in the initial development of ECs. A stronger cold advection for ECs increases upstream static stability, leading to intrusion of higher PV along the steeper isentropic surfaces. The importance of cold advection is further proved by numerical experiments with the Weather Research and Forecast (WRF) model on a typical winter EC. The weakening of cold advection within low-troposphere in sensitivity experiment can significantly decrease PV and stop the cyclone from explosive deepening. In addition to the consensus that diabatic processes play important roles in the intensification of explosive cyclogenesis, this study emphasizes the importance of horizontal cold advection (which is also associated with baroclinic instability) in the preconditioning PV for explosive cyclogenesis.

Corresponding author: Ping Lu, luping@mail.tsinghua.edu.cn

¹ State Key Laboratory of Severe Weather, Chinese Academy of Meteorological Sciences, Beijing 100081, China

² Ministry of Education Key Laboratory for Earth System Modeling, Department of Earth System Science, and, Joint Center for Global Change Studies, Tsinghua University, Beijing 10084, China

³ College of Oceanography and Meteorology, South China Sea Institute of Marine Meteorology, Guangdong Ocean University, Zhanjiang, 524088, China

⁴ Collaborative Innovation Center on Forecast and Evaluation of Meteorological Disasters/Key Laboratory of Meteorological Disasters of Ministry of Education, Nanjing University of Information Science and Technology, Nanjing 210044, China

⁵ College of Atmospheric Sciences, Chengdu University of Information Technology, Chengdu 610225, China

19 **1 Introduction**

20 The East Asian coast separates the largest continent and ocean on the earth, Eurasia and Pacific (Fig.1a). In
21 winter, ocean currents transport warm sea water northeastward, which releases a large amount of sensible heat
22 into atmosphere. Meanwhile, the climatology temperature trough is in the upstream of geopotential height
23 (GPH) trough in almost the whole troposphere (Fig.1b–d), which frequently brings cold air from high
24 latitudes. The large thermal contrast over this area cooperating with midlatitude westerly produces strong
25 baroclinic instability and many cyclones. On the other hand, the East Asia is one of the most densely
26 populated area with many flourishing ports, including Shanghai, Hongkong, Busan and Yokohama. Marine
27 transportation security is threatened by cyclones in this region, especially the rapidly enhanced ones, which
28 are usually referred to as the explosive cyclones (ECs).

29 ECs, also known as meteorological bombs, often pose challenges in forecasting and significant threats to
30 human life and property (Rice 1979; Lamb 1991; Liberato et al. 2011; Liberato et al. 2013) so as to receive
31 considerable attention. The landmark study of Sanders and Gyakum (1980) defined them as the extratropical
32 cyclones with central sea-level pressures (SLPs) fall at least 24 hPa a day when adjusted geostrophically to
33 60 °N. This criteria for ECs was modified by following studies to consider lower latitudes of EC
34 occurrence (Roebber 1984; Gyakum et al. 1989; Yoshida and Asuma 2004; Zhang et al. 2017), shorter time
35 interval of pressure fall (Petty and Miller 1995; Yoshida and Asuma 2004; Zhang et al. 2017), and maximum
36 wind speed at 10 m (Fu et al. 2020), which may lead to statistical variations, yet nearly all the related studies
37 (Chen et al. 1992; Wang and Rogers 2001; Lim and Simmonds 2002; Yoshida and Asuma 2004; Zhang et al.
38 2017; Fu et al. 2020) marked the offshore East Asia as one of the most frequent areas for explosive
39 cyclogenesis.

40 The explosive deepening of cyclones is considered closely related to multiple dynamic and
41 thermal-dynamic characteristics of the synoptic and marine background. The warm ocean current produces
42 large sea surface temperature (SST) gradient, transporting sensible and latent heat to atmosphere while
43 lowering its stability (Kuвано-Yoshida and Asuma 2008; Taguchi et al. 2009; Kuвано-Yoshida and Enomoto
44 2013). The upper-level jet stream provides dynamic forcing on the left side of its exit with strong divergence,
45 positive vorticity advection and lifting (Uccellini and Kocin 1987; Wash et al. 1988; Cammas and Ramond
46 1989; Nakamura 1993). The upper-air trough leads a downstream positive vorticity advection, and the
47 strength of upper-level vorticity advection is closely related to the deepening rate of cyclones (Sanders 1986).
48 The strong baroclinicity is also an important factor that drives explosive cyclogenesis (Sanders 1986;
49 Manobianco 1989; Wash et al. 1992), and enhancement of the low-level baroclinicity leads to increase of ECs
50 over northwest Pacific in winter in the past 30 years (Iwao et al. 2012).

51 To consider both the dynamic and thermal-dynamic factors, the potential vorticity (PV) was analyzed in
52 many studies. A number of case studies (e.g., Davis and Emanuel 1988; Kuo et al. 1991; Campa and Wernli
53 2012) showed that the upper-tropospheric PV was associated with the development of low-level cyclogenesis,
54 and there were three distinct positive PV anomalies in an extratropical cyclone: surface, lower-tropospheric,
55 and upper-tropospheric PV anomalies. Downward transport of the high PV in stratosphere effectively
56 enhances the downstream surface cyclones (Bosart and Lin 1984; Reader and Moore 1995). The low-level PV
57 anomaly coupled with upper-level PV disturbance can induce the rapid deepening of cyclones (Cordeira et al.
58 2011). The diabatic process (i.e., the local PV generation) is also notable. Heo et al. (2015) showed that the
59 latent heat release (LHR) in warm conveyor belt produces nearly half of the low-level PV generation during
60 initial development of a spring EC. Using idealized simulation, Schemn and Wernli (2014) proved that the

61 LHR strengthens PV anomaly, leading to speed-up of both the surface wind and upper-level jet stream. A
62 climatological analysis by Binder et al. (2016) indicated that the impact of LHR depends on the location of
63 PV generation.

64 Despite the above studies on the impacts and relative contributions of different physical processes on ECs,
65 the physics and underlying mechanisms that distinguish ECs from ordinary cyclones (or nonexplosive
66 cyclones; OCs) was rarely discussed. For example, many studies emphasize the importance of LHR as an
67 important source of low-level PV anomaly in ECs, we notice it is the same for many OCs as well, therefore
68 detailed systematic comparisons of ECs versus OCs are needed to quantify the causes of explosive
69 cyclogenesis. Following this motivation, this study presents detailed comparison of winter ECs versus OCs in
70 the perspective of potential vorticity (PV) using 10 years of reanalysis data with high temporal and spatial
71 resolutions in East Asia. The paper is organized as follows. Section 2 describes the data, methods and WRF
72 model configuration. Section 3 shows the systematic comparison of ECs vs OCs based on reanalysis data,
73 including characteristics in cyclone intensity, low-level baroclinicity, and decomposition of local PV tendency.
74 Findings in Section 3 is further proved by WRF experiments in Section 4. A summary is given in Section 5.

75 **2 Data and methods**

76 **2.1 Data**

77 This study uses the 5th generation of the European Centre for Medium-Range Weather Forecasts (ECMWF)
78 Reanalysis (ERA5; available at <https://cds.climate.copernicus.eu>) to identify the cyclones and analyze their
79 dynamic and thermal-dynamic structures. The dataset has a high temporal resolution of 1 h, a high horizontal
80 resolution of 0.25°, and 37 vertical layers. It covers 10 winters, which are Decembers, Januaries, and

81 Februaries of 2010–2019. The ERA5 reanalysis is also used to generate the initial and boundary conditions
82 for the numerical simulations.

83 The cloud images retrieved from 10.3 μm far-infrared observation of the satellite of Himawari-8 (available
84 at <https://himawari8.nict.go.jp/>) are used to show the development of cloud around the EC discussed in
85 Section 4.

86 **2.2 Algorithms for statistical analysis**

87 This study tries to identify all the winter cyclones happened over the East Asia (defined by the region within
88 20–50 °N, 105–155 °E, shown by Fig. 1a) during 2010–2019. The detection and tracking method follow Hart
89 (2003) and have been modified according to the high temporal and spatial resolution of ERA5 dataset.

90 To detect cyclones at each moment, SLP distribution is shown by contours starting at 900 hPa with an
91 interval of 2.5 hPa. A cyclone is considered to exist when there is at least one close isobaric line within a
92 circular area with radius of 800 km and the local minimum of SLP less than 1020 hPa. The location of the
93 lowest SLP is considered as the cyclone center. This circular area with radius of 800 km is larger than the
94 5°×5° box checked by Hart (2003) to find more cyclones, especially during their initial development.

95 To track cyclones, the nearest two cyclones with 1-h interval are considered as the same cyclone when their
96 distance is less than 500 km. Such a long threshold ensures that a wide but shallow cyclone is not falsely
97 identified as two or more cyclones when SLP around its center rapidly decreases. Finally, the cyclones whose
98 appearances over the East Asia last less than 24 h are dismissed, which include those with short lifetimes as
99 well as those move away from this region.

100 The priority of this method is to find as many cyclones as possible with a low computational cost when
 101 dealing with such a long-term data with high resolution. It gives reasonable results, and small changes in the
 102 thresholds do not affect conclusions of this study.

103 The definitions of EC by former studies often use deepening rate (DR) of the form

$$104 \quad DR_{\delta t} = \frac{p_{t-\delta t/2} - p_{t+\delta t/2}}{\delta t} \cdot \frac{\sin \varphi_0}{\sin \frac{\varphi_{t-\delta t/2} + \varphi_{t+\delta t/2}}{2}} \quad (1)$$

105 where δt is time interval, p is central SLP and φ is latitude. The fraction of sine functions denotes the
 106 geostrophic adjustment, with φ_0 denotes the standard latitude. Following Zhang et al. (2017), this study lets
 107 $\varphi_0=45^\circ$, and defines ECs as the cyclones with 12-h deepening rate (DR_{12}) of ≥ 1 hPa/h. ECs can be classified
 108 into 4 ranks according to DR_{12} : weak ($1.00 \leq DR_{12} \leq 1.29$ hPa/h), moderate ($1.30 \leq DR_{12} \leq 1.69$ hPa/h), strong
 109 ($1.70 \leq DR_{12} \leq 2.29$ hPa/h), and super ($DR_{12} \geq 2.30$ hPa/h) ECs.

110 This study also calculates the 1-h deepening rate (DR_1) to analyze the short-term variation, and calculates
 111 the 36-h deepening rate (DR_{36}) to consider the development of a cyclone during the whole simulation
 112 period. Synthetic analysis is used to show the characteristics of ECs and OCs. For a category of cyclones, the
 113 distribution of each variable is averaged among all the cases in relative geographic coordinates within a
 114 $20^\circ \times 20^\circ$ square domain around the centers. Anomaly for potential temperature and GPH is analyzed to
 115 eliminate the impact of different latitudes, which is defined as the difference between a value at any grid point
 116 and its average of the $20^\circ \times 20^\circ$ square domain at the same pressure level.

117 This study measures the low-level baroclinic instability by the Eady growth rate (E_g ; Hoskins and Valdes
 118 1990), which is defined by

$$119 \quad E_g = 0.31 f \left| \frac{\partial v}{\partial z} \right| N^{-1} \quad (2)$$

120 where f is the Coriolis parameter, \mathbf{v} is the horizontal wind velocity, z is the GPH, g is the gravitational
 121 acceleration, and N is the Brunt-Väisälä frequency. According to the thermal-wind effect, the vertical shear of
 122 wind velocity is closely related to the horizontal gradient of air temperature. N is a measurement of static
 123 stability. Definition of EGR is consistent with the concept that strong thermal contrast and static instability
 124 produce strong baroclinicity. Following Seiler and Zwiers (2016), EGR is computed by daily values between
 125 850 and 700 hPa.

126 The decline rate of potential temperature (Γ) is calculated by

$$127 \quad \Gamma = -\frac{\partial\theta}{\partial p} \quad (3)$$

128 where θ is potential temperature and p is pressure. Γ is used to analyze the static stability, since it is more
 129 straightforward than N and is a part of PV.

130 The Ertel PV is calculated by

$$131 \quad \text{PV} = g\Gamma(\zeta_\theta + f) \quad (4)$$

132 where ζ_θ is the relative vorticity on isentropic surface. PV is conserved following the adiabatic motion in the
 133 absence of friction and thus provides the balance between ζ_θ (the strength of cyclone), f (i.e., latitude), and the
 134 static stability.

135 The local PV tendency ($\frac{\partial\text{PV}}{\partial t}$) can be decomposed to three terms by only considering the diabatic PV
 136 modification (i.e., neglecting the surface friction effect):

$$137 \quad \frac{\partial\text{PV}}{\partial t} = -\mathbf{v} \cdot \nabla\text{PV} - \omega \frac{\partial\text{PV}}{\partial p} + J_{\text{PV}} \quad (5)$$

138 where ω is the descending speed in pressure coordinate, and J_{PV} is diabatic variation of PV. The three terms on
 139 the right-hand side are the horizontal PV advection, the vertical PV transport and the diabatic term

140 respectively. Consider a quasi-cubic zone around the cyclone center with x ranging from x_1 to x_2 , y ranging
 141 from y_1 to y_2 and p ranging from p_1 to p_2 ($p_1 < p_2$), average values of the PV tendency, advection and vertical
 142 transport within it can be calculated by

$$143 \quad \frac{\partial \text{PV}}{\partial t} = \frac{1}{g \delta m} \int_{p_1}^{p_2} \int_{y_1}^{y_2} \int_{x_1}^{x_2} \frac{\text{PV}(x, y, p, t + \delta t) - \text{PV}(x, y, p, t - \delta t)}{2\delta t} dx dy dp \quad (6)$$

$$144 \quad -\mathbf{v} \cdot \nabla \text{PV} = \frac{1}{g \delta m} \left\{ \int_{p_1}^{p_2} \int_{y_1}^{y_2} [u(x_1, y, p, t) \text{PV}(x_1, y, p, t) - u(x_2, y, p, t) \text{PV}(x_2, y, p, t)] dy dp \right. \\ \left. + \int_{p_1}^{p_2} \int_{x_1}^{x_2} [v(x, y_1, p, t) \text{PV}(x, y_1, p, t) - v(x, y_2, p, t) \text{PV}(x, y_2, p, t)] dx dp \right\}$$

145 (7)

$$146 \quad -\omega \frac{\partial \text{PV}}{\partial p} = \frac{1}{g \delta m} \int_{y_1}^{y_2} \int_{x_1}^{x_2} [\omega(x, y, p_1, t) \text{PV}(x, y, p_1, t) - \omega(x, y, p_2, t) \text{PV}(x, y, p_2, t)] dx dy$$

147 (8)

148 where δt is the time interval of data, and δm is the air mass within this zone, which is calculated by

$$149 \quad \delta m = \frac{1}{g} \int_{p_1}^{p_2} \int_{y_1}^{y_2} \int_{x_1}^{x_2} dx dy dp \quad (9)$$

150 After the 3 terms are identified by Equations 6–8, J_{pv} can be approximated by the residual of Equation 5.

151 2.3 Simulation design

152 To analyze the initial development of an EC happened in Dec 2017 and the factors that affect its explosive
 153 deepening, a series of simulation experiments are done using the Advanced Research WRF model ([Skamarock
 154 et al., 2008](#)) Version 3.9.1. According to the cyclone track, the model domain covers most of the East Asia
 155 (Fig.2) with 201×151 grid points and a horizontal resolution of 20 km, and no nesting is adopted. Simulation
 156 starts at 0000 UTC 23 Dec, more than 12 h before the cyclone was initiated, and lasts for 48 h, leaving the
 157 first 12 h for spin-up. All the simulations apply the Kain-Fritsch cumulus scheme ([Kain, 2004](#)), the Yonsei
 158 University (YSU) planetary boundary layer (PBL) scheme ([Hong et al., 2006](#)), the Thompson microphysics

159 scheme (Thompson et al., 2008), the Rapid Radiative Transfer Model for Global climate model (RRTMG)
160 shortwave and longwave radiation scheme (Iacono et al., 2008), and the Noah land surface model (Tewari et
161 al., 2004). Details of the model configuration are shown in Table 1.

162 The initial and boundary conditions are derived from ERA5 reanalysis. A control experiment (Exp-Ctrl)
163 and 4 sensitivity experiments are designed, with the purposes shown in Section 4. In Exp-MH (short for
164 “modifying humidity”), the background relative humidity is cut in half. In Exp-SST, SST is decreased by 4 °C.
165 In Exp-MT (short for “modifying temperature”), the background temperature between 500 hPa and 850 hPa
166 with i ranging from 1 to 150 and j ranging from 51 to 150 (shown by the pink frame in Fig.2) is increased by
167 $4 \times (j-50)/100$ °C (where ij is the grid number in zonal/meridional direction). Exp-MH and Exp-SST modify
168 the whole initial and boundary conditions, while Exp-MT only modifies the northwest part of them.
169 Exp-MT+MH does the modifications of both Exp-MH and Exp-MT. A Comparison of 4 experiments is
170 shown in Table 2.

171 **3 Statistical analysis**

172 135 cyclones are identified which stay over the East Asia for at least 24 h. As shown in Figure 3, only ~17%
173 of them are initiated over land, and almost all of the explosive cyclogenesis start over sea. The average 24-h
174 tracks for OCs and different ranks of ECs distribute around the Japan Island, and are quite close to the areas
175 of Kuroshio and Tsushima Warm Current (Fig.1a). Cyclones with higher deepening rates have a further south
176 average initial location, indicating that the explosive cyclogenesis might be related to deeper GPH trough in
177 the mid-troposphere, higher SST and more adequate water vapor.

178 To compare the initial development of OCs and ECs, their intensities and deepening processes are analyzed.

179 Then characteristics of the synoptic background are compared, focusing on the differences in atmospheric

180 baroclinicity. Finally, PV structures are compared, and the reason for their difference is discussed.

181 **3.1 Cyclone intensity**

182 As shown in Figure 4a, 63 out of the 135 cyclones are OCs, which means more than half of the winter

183 cyclones went through explosive growth. 37.5/36.1/20.8/5.6% of the 72 ECs are ranked as the

184 weak/medium/strong/super ECs, indicating a higher proportion for stronger ECs than Zhang et al. (2017) with

185 the same methods, which gives a percentage of 65.1/29.1/3.9/1.9% over Sea of Japan and 45.6/33.2/18.6/2.6%

186 over Northwest Pacific (Fig.1a). Zhang et al. (2017) analyze ECs from October to April during 2000–2015

187 using $1^\circ \times 1^\circ$ reanalysis. A colder season in this study is more beneficial to stronger cyclogenesis, and

188 high-resolution reanalysis data could increase the climatological frequency of ECs (Allen et al., 2010). Except

189 the Super ECs, average central SLPs for other ranks are quite similar at initial time (Fig.4b), when the strong

190 ECs have a higher central SLP than other cyclones. Meanwhile, stronger ECs have higher deepening rate for

191 the whole time, and their explosive growths start earlier. It is notable that the maximum wind speed varies

192 according to the central SLP (Fig.4b–c), and although a higher deepening rate leads to a faster decrease of

193 central SLP, it is not a guarantee for stronger surface wind. Fu et al. (2020) choose a wind speed of 17.2 m s^{-1}

194 as the threshold value in the definition of ECs, since the major threat of cyclones to shipping safety is due to

195 strong wind.

196 **3.2 Low-level baroclinicity**

197 The synoptic backgrounds for ECs have stronger low-level baroclinicity than OCs. As shown in Figure 5, at

198 initial time, OCs usually have an upper-air GPH trough upstream, and the geostrophic wind is almost parallel

199 to isotherms at 500 hPa. The low-level troughs are located closer to the cyclone centers, and the zonal
200 temperature gradients are larger at 850 and 925 hPa. This thermal-dynamic structure (Fig.5a–c) shows that the
201 strong cold/warm advections in the west/east of the cyclone centers exists within low-troposphere. Zonal
202 thermal contrast is larger for ECs, with the temperature difference between east and west boundaries 2–3 K
203 larger than OCs (Fig.5d–f), and the maximum difference is located $\sim 6^\circ$ north of the centers. GPH anomalies
204 are lower around centers and higher in the east and west at 850 and 925 hPa, indicating deeper troughs and
205 stronger heat advections within low-troposphere. The typical characteristics for cyclones also include
206 upper-level jet streams with maximum speed of $\sim 50 \text{ m s}^{-1}$ (Fig.5g) and abundant water vapor along the warm
207 conveyor belt (Fig.5h). For ECs, the wind speed is $\sim 4 \text{ m s}^{-1}$ larger in the upper-level jet streams (Fig.5i), and
208 precipitable water is $\sim 3 \text{ mm}$ more in the south (Fig.5h).

209 The stronger heat advection and zonal thermal contrast in the low-troposphere for ECs leads to stronger
210 low-level baroclinicity. As shown in Figure 6a, the low-troposphere has a much weaker static stability over
211 sea than land, with a warmer surface in winter. The average Γ decreases from southwest to northeast. It is
212 above $7 \times 10^{-4} \text{ K Pa}^{-1}$ over the East China Sea and most of the Yellow Sea, and below $6 \times 10^{-4} \text{ K Pa}^{-1}$ over the
213 Sea of Japan and the North Pacific Ocean where the average E_g is above 1 d^{-1} . Both the weak static stability
214 and the strong baroclinicity is beneficial to the cyclogenesis, which is an explanation for most winter cyclones
215 going through these regions (Fig.3). During initial development of OCs, large E_g exists within ± 4 latitudes
216 around centers (Fig.6b), and is more widely distributed in the east (since the warm shear zone is usually larger
217 than the cold shear zone), while Γ is smaller around the center (since the warm tongue around center enhances
218 with pressure as shown in Fig.5a–c). Both variables are larger for ECs (Fig.6c). With stronger cold advection,
219 E_g increases by $>0.2 \text{ d}^{-1}$ in the southwest, and its maximum value near the cold shear is pushed southward. Γ

220 increases significantly in the same area, and the maximum increment exists in the south of the west boundary,
221 leading to a larger difference of static stability between center and west for ECs. This is quite important for
222 the explosive cyclogenesis, which is discussed in Section 3.3.

223 **3.3 PV budget**

224 Since the relative vorticity of horizontal wind reflects the dynamic strength of cyclones, its enhancement is
225 closely related to cyclogenesis. As indicated by Equation 4, relative vorticity is associated with PV, f and
226 geostrophic vorticity (which varies a little in the region this study focuses on). Static stability is stronger for
227 ECs during initial development (as shown in Section 3.2), so that their stronger relative vorticity may result
228 from a higher initial PV.

229 As shown in Figure 7, there is a PV intrusion in the west of cyclones, which is stronger for ECs than OCs.
230 For OCs, the initial PV is <1 PVU ($1 \text{ PVU} = 1 \times 10^{-6} \text{ m}^2 \text{ s}^{-1} \text{ K kg}^{-1}$) around center, and increases to >1.2 PVU
231 within 12 h (Fig.7a–c). A high PV tongue extends downwards in the west, making the mid-troposphere have
232 much higher PV in the west than east. When the mid-latitude westerly with cold air from Eurasia meets
233 low-level perturbation with warm air, the descending is accelerated according to down-curved isotherms,
234 transporting high PV from upper air to the perturbation. The enhancement of local PV (i.e., horizontal and
235 vertical PV transport, diabatic PV production) and the weakening of static stability along the motion from
236 upstream to cyclone center (Fig.6b) can increase the local relative vorticity, which is increased by $\sim 50\%$
237 around the center within 12 h. For ECs, the local PV increase is stronger (Fig.7d–f). At initial time, there is a
238 stripe starting over the center and inclining to the west where PV is higher for ECs. PV increases by $\sim 30\%$
239 over center and at 500 hPa near the west boundary. The positive increment grows larger during initial
240 development, and PV within 300–850 hPa is significantly higher for ECs in the west at 12 h. The pattern of

241 relative vorticity difference is quite similar to PV difference at mid-low levels, indicating the useful
242 manifestation of PV in explosive cyclogenesis analysis. Note that for both categories of cyclones, PV around
243 center is higher than low-troposphere PV in the west even at initial time, indicating that PV advection around
244 center is negative, and PV generation by diabatic process is an important term in cyclogenesis, which is
245 consistent with former studies (e.g., Heo et al., 2015; Schemn and Wernli, 2014).

246 The local PV tendency is analyzed to further discuss the origin of PV transport. The 4 terms in Equation 5
247 are calculated in a quasi-cubic box within 500–950 hPa over the $20^{\circ}\times 20^{\circ}$ square domain around the center for
248 each cyclone by Equations 6–9. As shown in Figure 8, the PV advection dominates the enhancement of PV.
249 During the first 3 h, PV tendencies are close for both categories, but the adiabatic change (defined as the
250 summation of advection and vertical transport) for ECs is larger than OCs (Fig.8a), with a larger positive
251 advection term and a larger negative vertical transport term (Fig.8b). The advection term keeps increasing for
252 ECs and varies little for OCs in the next 18 h (Fig.8b), accompanied by the increasing difference of PV
253 tendency (Fig.8a). At 21 h, both the PV tendency and advection term for ECs are ~ 4 PVU/h larger than OCs.
254 The vertical transport term varies with opposite trend to advection term, indicating that higher PV is
255 converged into the box by horizontal airflow and is diverged by lifting. The net diabatic term over the column
256 is negative for OCs as the diabatic PV erosion above the maximum heating level may suppress the diabatic
257 PV production below. The net diabatic PV is enhanced within ECs due to their stronger LHR, but the
258 difference is not apparent before 10 h (Fig.8b) when the total PV tendency for ECs is already 1 PVU/h larger
259 than OCs (Fig.8a), indicating that the enhancement of diabatic PV production is a result rather than the cause
260 of the initial enhancement of PV. The correlation between PV advection and PV tendency is >0.8 (Fig.8c),
261 much stronger than others (Fig.8d–e), further proving the crucial role of PV advection.

262 According to Equation 7, the net horizontal PV advection over a quasi-cubic box can be decomposed to 4
263 terms, which denote the transport of PV across the box's four lateral boundaries. As shown by Figure 9, the
264 most significant difference of PV transport exists at the west boundary, where west wind flow brings higher
265 PV into the box for ECs. Since the zonal wind is only 1–2 m s⁻¹ stronger, the main reason for the stronger PV
266 intrusion is a higher low-troposphere PV in the west (Fig.7). The difference is also evident at the north
267 boundary (Fig.9d), which offsets part of the enhancement of PV input at the west boundary (note that a
268 positive difference of $v \cdot PV$ here means higher PV output from the box). Thus, the stronger input of PV in the
269 west of cyclones is the key cause for the higher PV within the ECs.

270 As shown in Figure 10, the invasion of colder air leads to a more stable stratification in the west for ECs
271 (Fig.6c), which leads to the stronger PV intrusion. The meridional thermal contrast is ~3 K stronger within 20
272 latitudes at initial time (Fig.10a). The colder air moves southward while sinking (Fig.10b), which significantly
273 enhances the static stability in the southwest (Fig.6c). Since the stabilities around center are quite similar
274 (Fig.6c), slope of the isentropic has to be steeper in the west for ECs. Higher PV is transported downward
275 adiabatically along isentropic surfaces (note that upper-air PV is much higher than low-level). Comparison
276 between Figure 9a and Figure 10b show that the higher PV mainly exists above the levels where colder air
277 invades.

278 Figure 11 shows the development of a cyclone from a PV perspective. The initiation and deepening of a
279 cyclone can be attributed to the enhancement of PV around the cyclone center, which is impacted by both
280 adiabatic and diabatic processes. The adiabatic process is the key cause for the initial development of a higher
281 PV for ECs. Compared to OCs, there is a stronger upstream perturbation within low-troposphere for ECs,
282 which brings colder air. The colder advection increases upstream static stability, so that PV from higher levels

283 is transported downward along steeper isentropic. Meanwhile, the stronger stability in the west makes the
284 stretching of air parcel more significant while moving eastward, so that the vorticity is further enhanced. The
285 diabatic process includes the sensible heat flux from underlying surface, latent heat absorption and release by
286 moist processes. The net diabatic PV modification is stronger for ECs resulting from ECs' stronger LHR, the
287 evident difference only starts after $t=10$ h, indicating that diabatic effect is probably a result rather than the
288 cause for the initial higher PV. The next section tries to prove the impact of the cold advection based on
289 numerical simulation, and compare it with other factors related to diabatic, such as background humidity and
290 SST.

291 **4 Numerical experiments**

292 The EC case was initiated over the Yellow Sea and rapidly deepened while moving northeastward off East
293 Asia coast during 23–24 Dec 2017. As shown in Figure 12, a surface inverted trough existed over the East
294 China coast (Fig.12m) with a 500 hPa GPH trough upstream (Fig.12e) at 1200 UTC 23 Dec, when thick
295 clouds covered both onshore and offshore regions (Fig.12a). Southeastward air flow within low-troposphere
296 brought cold air from high latitudes (Fig.12i). A cyclone appeared within 12 h with central SLP lower than
297 1010 hPa (Fig.12n). When moving over the Sea of Japan, the cyclone rapidly deepened (Fig.12o–p) with
298 deeper low-level trough (Fig.12.k–l), and the surface wind speed increased beyond 20 m s^{-1} . The hook-shaped
299 cloud system accompanied by appearance of the cyclone is a result of the cooperation of cold air and warm
300 conveyor belt (Fig.12b), and it can be told from the widespread marine cold-flow-clouds left by the cyclone
301 that the cold advection is very strong.

302 The detailed simulation design is shown in Section 2.3. Other than Exp-Ctrl, each sensitivity experiment
303 weakens 1 or 2 processes related to the explosive cyclogenesis. Exp-MH decreases the water vapor, so that

304 LHR is decreased. Exp-SST cools the sea surface, decreasing the sensible heat. Both experiments show the
305 impact of diabatic process. Exp-MT weakens the cold advection by warming the upstream air in
306 low-troposphere, which can decrease the upstream static stability and weaken the downward transport of high
307 PV. Note that modifications by Exp-MH and Exp-SST are very exaggerated, while modification by Exp-MT
308 is consistent with the difference of thermal structure between ECs and OCs, since it decreases the meridional
309 temperature gradient by 4 K within ~20 latitudes (Fig.10b).

310 **4.1 Evaluation of simulation**

311 Both Exp-Ctrl and Exp-MH reproduces the cyclone development quite close to reanalysis. As shown in Figure
312 2, for Exp-Ctrl, Exp-MH, Exp-SST and ERA5, the cyclone tracks are similar showing a northeastward
313 movement from the Yellow Sea to the Sea of Japan, while cyclones for Exp-MT and Exp-MT+MH move
314 eastward to the Japan Islands. The average 36-h deepening rate is 1.31 hPa h^{-1} for ERA5 during simulation
315 period, which is only 0.03 and 0.04 hPa h^{-1} less for Exp-Ctrl and Exp-MH, and much less for the other 3
316 experiments (Fig.13a). For Exp-MT and Exp-MT+MH, the cyclogenesis is weaker for the whole time, while
317 for Exp-SST, the difference is apparent after 16 h (0600 UTC 24 Dec; Fig.13b). Maximum wind speed for the
318 3 experiments is also smaller than others (Fig.13b). In summary, the control experiment reasonably
319 reproduces the development of this winter EC, and both Exp-MT and Exp-MT+MH can significantly slow
320 down the cyclogenesis, indicating the importance of the upstream cold advection in low-troposphere.
321 Exp-SST has a similar effect, which proves contribution of the warm sea surface in winter and explains why
322 most explosive cyclogenesis happens over sea.

323 **4.2 PV tendency**

324 To analyze the impacts of modifications by sensitivity experiments, again each term in Equation 5 is
325 calculated within 500–950 hPa over the dashed frame in Figure 2 by Equations 6–9. As shown in Figure 14,
326 compared to Exp-Ctrl, Exp-MT and Exp-MT+MH significantly decreases the PV tendency (Fig.14a) by
327 decreasing the PV advection, since their advection terms are 3–4 PVU h⁻¹ larger than Exp-Ctrl before 10 h
328 (Fig.14b). Their diabatic terms are similar to Exp-Ctrl before 15 h, and are smaller after that (Fig.14c), since
329 their weaker cyclones cannot produce as much LHR. This indicates a nonnegligible impact of PV advection
330 on diabatic process during cyclogenesis. PV tendency for Exp-SST is slightly larger before 16 h and much
331 smaller after that (Fig.14a), and the change mainly comes from the diabatic term (Fig.14c). Note that the early
332 enhancement is due to a stronger static stability near sea surface with lower SST, and thus is not related to
333 stronger vorticity or lower central SLP (Fig.13b). Modifying water vapor makes little difference in PV
334 tendency. The diabatic term for Exp-MH is smaller than Exp-Ctrl, while that for Exp-MT+MH is larger than
335 Exp-MT (Fig.14c), indicating a weak and complicated relationship between water vapor transport and PV
336 generation.

337 **4.3 Humidity structure**

338 Many studies have proved that LHR is important for PV generation and explosive cyclogenesis. Heo et al.
339 (2015) shut down the cumulus parameterization and diabatic heating in microphysics scheme in sensitive
340 experiment, and showed that ~50% of the low-level PV generation is contributed by LHR for an EC case.
341 Interestingly, Exp-MH cut the water vapor by half over the whole domain but only slightly changed the PV
342 tendency and deepening rate. As shown in Figure 15, the water vapor content around cyclone center is
343 dominated by the strength of cyclone rather than the background humidity. The precipitable water is lower
344 than 10 mm over land, ~16 mm around center and higher than 30 mm in the warm conveyor belt for Exp-Ctrl

345 (Fig.15a–e). Although the southeast of cyclone is much drier for Exp-MH, its precipitable water around center
346 is not decreased much. Strong convergence still brings much water vapor into the cyclone. Meanwhile, the
347 movement of cyclone for Exp-MT+MH is behind Exp-MT, making its vapor content around center decrease
348 (Fig.15l–n, q–s), leading to a larger difference between Exp-MT+MH and Exp-MT than Exp-MH and
349 Exp-Ctrl (Fig.13a). These comparisons show that the strengthen of cyclone decides the transport of water
350 vapor, and thus the LHR (which is closely related to water vapor content). It again proves stronger diabatic
351 process is a result rather than the cause for winter ECs initiation over this region.

352 Results of the numerical experiments on this winter EC emphasize the important role of cold advection on
353 the intrusion of upper-air PV, which is consistent with statistical analysis. For ECs, the upstream meridional
354 thermal contrast is ~4 K stronger than OCs in average within 20 latitudes during initial development (Fig.10b).
355 Exp-MT shows that this winter EC is weakened into an OC if the difference is taken away. Meanwhile, the
356 background humidity has a weak and complicated impact on PV generation.

357 **5 Conclusion**

358 ECs frequently show up off the East Asian coast in winter and cause great casualties and property loss. To
359 analyze the main reason for explosive cyclogenesis that makes ECs different from other cyclones, this study
360 compares the initial developments between ECs and OCs in 10 winters during 2010–2019, based on the
361 hourly ERA5 reanalysis with a high horizontal resolution of 0.25°.

362 135 cyclones are identified which stay over the East Asia for at least 24 h, and 72 of them went through
363 explosive deepening. 37.5/36.1/20.8/5.6% of the ECs are ranked as the weak/medium/strong/super ECs. In
364 decomposition of local PV tendency, our results show the dominant contribution of cold advection (with
365 correlation coefficient of 0.8). On the other hand, even though diabatic process contributes a lot to PV

366 generation for ECs (e.g., Schemm and Wernli, 2014; Heo et al., 2015; Binder et al., 2016), it might have a
367 similar impact on OCs than ECs (as indicated by a correlation coefficient of 0.3). and is not the key cause for
368 explosive cyclogenesis. For ECs, the low-level cold advection is stronger, with the temperature gradient
369 $\sim 0.002 \text{ K km}^{-1}$ larger than that for OCs at the lateral boundary 10 longitudes west of cyclone centers. It
370 increases upstream static stability, so that stronger PV intrusion occurs along the steeper isentropic, which
371 enhances the PV advection. The stronger stability in the west makes the stretching of air parcel more
372 significant while moving eastward, so that the vorticity is further enhanced.

373 The impact of cold advection on PV advection and explosive cyclogenesis is further proved by a series of
374 numerical experiments on a typical EC initiated over the Yellow Sea and explosively deepened during 23–24
375 Dec 2017. Simulation by WRF model reasonably reproduces the development of this EC with the 36-h
376 deepening rate only 0.03 hPa h^{-1} lower than reanalysis. A sensitivity experiment roughly took away the
377 temperature gradient difference between ECs and OCs by decreasing the gradient by 0.002 K km^{-1} , and
378 significantly weakened the EC with deepening rate decreased by 0.32 hPa h^{-1} . The weakening of cold advection
379 decreased the PV advection and thus the PV tendency. Meanwhile, modification of the background humidity
380 only slightly changed the PV tendency and deepening rate, since water vapor content and LHR around center
381 are dominated by dynamic strength of cyclone rather than background humidity. A decrease of 4 K in SST can
382 also weaken the EC by decreasing the diabatic term, which explains why most explosive cyclogenesis happens
383 over warm sea. In reality, SST varies very little among cyclones in winter, and cannot be used to distinguish
384 ECs.

385 In addition to the consensus that diabatic processes play crucial roles in the explosive cyclogenesis, this
386 study emphasizes the importance of horizontal cold advection (which is also associated with baroclinic

387 instability) in the initial enhancement of PV and thus the ‘preconditioning’ of preexisting (or antecedent) PV
388 for later rapid deepening development of explosive cyclogenesis. This is achieved in two ways: the
389 preconditioning PV (1) directly provides relative vorticity and (2) indirectly makes the diabatic PV production
390 (which is proportional to the vertical gradient of diabatic heating and the background PV) more efficient at a
391 later stage. With the limitation in data sources, large uncertainties still exist in the estimation of vertical PV
392 transport and diabatic PV production, which will be evaluated in our ongoing studies.

393

394 **Acknowledgements** We would like to thank anonymous reviewers for their helpful comments and
395 suggestions that improved the manuscript.

396 **Author contribution** Xiaoyu Gao designed the research and performed the analysis. Xiaoyu Gao and Ping Lu
397 wrote the paper. All the authors discussed the results and commented on the manuscript.

398 **Funding** This research has been funded by the National Natural Science Foundation of China (42005116,
399 41905071).

400 **Availability of data and material** The ERA5 reanalysis data are available at
401 <https://cds.climate.copernicus.eu>, and the cloud images of Himawari-8 are available at
402 <https://himawari8.nict.go.jp/>.

403 **Code availability** All the codes are programmed by NCAR Command Language and Matlab. The codes are
404 available and maintained by Xiaoyu Gao (anthas@126.com).

405 **Declarations**

406 **Ethics approval** Not applicable

407 **Consent to participate** Not applicable

408 **Consent for publication** Not applicable

409 **Conflict of interest** The authors declare no competing interests.

410

411 **References**

412 Binder H, Boettcher M, Joos H, Wernli, H (2016) The role of warm conveyor belts for the intensification of
413 extratropical cyclones in northern hemisphere winter. *J Atmos Sci* 73(10):3997–4020.

414 <https://doi.org/10.1175/JAS-D-15-0302.1>

415 Bosart L F, Lin S C (1984) A diagnostic analysis of the Presidents' Day storm of February 1979. *Mon Wea*
416 *Rev* 112(11):2148–2177. [https://doi.org/10.1175/1520-0493\(1984\)112<2148:ADAOTP>2.0.CO;2](https://doi.org/10.1175/1520-0493(1984)112<2148:ADAOTP>2.0.CO;2)

417 Cammas J P, Ramond D (1989) Analysis and diagnosis of the composite of ageostrophic circulations in
418 jet-front systems. *Mon Wea Rev* 117(11):2447–2462.

419 [https://doi.org/10.1175/1520-0493\(1989\)1172.0.CO;2](https://doi.org/10.1175/1520-0493(1989)1172.0.CO;2)

- 420 Chen F, Dudhia J (2001) Coupling an advanced land surface-hydrology model with the Penn State-NCAR
421 MM5 modeling system. Part I: model implementation and Sensitivity. *Mon Wea Rev* 129(4):569–585.
422 [https://doi.org/10.1175/1520-0493\(2001\)129.0.CO;2](https://doi.org/10.1175/1520-0493(2001)129.0.CO;2)
- 423 Chen S J, Kuo Y H, Zhang P Z, Bai Q F (1992) Climatology of explosive cyclones off the East Asian coast.
424 *Mon Wea Rev* 120(12):3029–3035. [https://doi.org/10.1175/1520-0493\(1992\)120.0.CO;2](https://doi.org/10.1175/1520-0493(1992)120.0.CO;2)
- 425 Cordeira J M, Bosart L F (2011) Cyclone interactions and evolutions during the “Perfect Storms” of late
426 October and early November 1991. *Mon Wea Rev* 139(6):1683–1707.
427 <https://doi.org/10.1175/2010MWR3537.1>
- 428 Fu G, Sun Y, Sun J, Li P (2020) A 38-year climatology of explosive cyclones over the northern hemisphere.
429 *Adv Atmos Sci* 37(2):143–159. <https://doi.org/10.1007/s00376-019-9106-x>
- 430 Gyakum J R, Anderson J R, Grumm R H, Gruner E L (1989) North Pacific cold-season surface cyclone
431 activity: 1975–1983. *Mon Wea Rev* 117(6):1141–1155.
432 [https://doi.org/10.1175/1520-0493\(1989\)117.0.CO;2](https://doi.org/10.1175/1520-0493(1989)117.0.CO;2)
- 433 Hart R E (2003) A cyclone phase space derived from thermal wind and thermal asymmetry. *Mon Wea Rev*
434 131(4):585–616. [https://doi.org/10.1175/1520-0493\(2003\)131<0585:ACPSDF>2.0.CO;2](https://doi.org/10.1175/1520-0493(2003)131<0585:ACPSDF>2.0.CO;2)
- 435 Heo K Y, Seo Y W, Ha K J, Park K S, Kim J, Choi J W, Jun K, Jeong J Y (2015) Development mechanisms
436 of an explosive cyclone over East Sea on 3–4 April 2012. *Dyn Atmos Oceans* 70:30–46,
437 <https://doi.org/10.1016/j.dynatmoce.2015.03.001>
- 438 Hong S Y, Noh Y, Dudhia J (2006) A new vertical diffusion package with an explicit treatment of
439 entrainment processes. *Mon Wea Rev* 134(9):2318–2341. <https://doi.org/10.1175/mwr3199.1>
- 440 Iacono M J, Delamere J S, Mlawer E J, Shephard M W, Clough S A, Collins W D (2008) Radiative forcing by
441 long-lived greenhouse gases: calculations with the AER radiative transfer models. *J Geophys Res Atmos*
442 113:D13103. <https://doi.org/10.1029/2008JD009944>
- 443 Iwao K, Inatsu M, Kimoto M (2012) Recent changes in explosively developing extratropical cyclones over
444 the winter Northwestern Pacific. *J Climate* 25(20):7282–7296.
445 <https://doi.org/10.1175/JCLI-D-11-00373.1>
- 446 Kain J S (2004) The Kain–Fritsch convective parameterization: an update. *J Appl Meteor* 43(1):170–181.
447 [https://doi.org/10.1175/1520-0450\(2004\)04360;0170:tkcpau62;2.0.co;2](https://doi.org/10.1175/1520-0450(2004)04360;0170:tkcpau62;2.0.co;2)
- 448 Kain J S, Fritsch J M (1990) A one-dimensional entraining/detraining plume model and its application in
449 convective parameterization. *J Atmos Sci* 47(23):2784–2802.
450 [https://doi.org/10.1175/1520-0469\(1990\)047.0.CO;2](https://doi.org/10.1175/1520-0469(1990)047.0.CO;2)
- 451 Kuwano-Yoshida A, Asuma Y (2008) Numerical study of explosively developing extratropical cyclones in
452 the Northwestern Pacific region. *Mon Wea Rev* 132(2):712–740.
453 [https://doi.org/10.1175/1520-0493\(2004\)132.0.CO;2](https://doi.org/10.1175/1520-0493(2004)132.0.CO;2)
- 454 Kuwano-Yoshida A, Enomoto T (2013) Predictability of explosive cyclogenesis over the Northwestern
455 Pacific region using ensemble reanalysis. *Mon Wea Rev* 141(11):3769–3785.
456 <https://doi.org/10.1175/MWR-D-12-00161.1>
- 457 Lamb H H (1991) *Historic Storms of the North Sea, British Isles and Northwest Europe*. Cambridge
458 University Press, Cambridge, pp 204p.
- 459 Liberato M L, Pinto J G, Trigo I F, Trigo R M (2011) Klaus—an exceptional winter storm over northern Iberia
460 and southern France. *Weather* 66(12):330–334. <https://doi.org/10.1002/wea.755>

- 461 Liberato M L R, Pinto J G, Trigo R M, Ludwig P, Ordóñez P, Yuen D, Trigo I F (2013) Explosive
462 development of winter storm Xynthia over the subtropical North Atlantic Ocean. *Nat Hazards Earth Sys*
463 *Sci* 13(9):2239–2251. <https://doi.org/10.5194/nhess-13-2239-2013>
- 464 Lim E P, Simmonds I (2002) Explosive cyclone development in the Southern Hemisphere and a comparison
465 with Northern Hemisphere events. *Mon Wea Rev* 130(9):2188–2209.
466 [https://doi.org/10.1175/1520-0493\(2002\)1302.0.CO;2](https://doi.org/10.1175/1520-0493(2002)1302.0.CO;2)
- 467 Lin Y L, Farley R D, Orville H D (1983) Bulk parameterization of the snow field in a cloud model. *J Climate*
468 *Appl Meteor* 22(6):1065–1092. [https://doi.org/10.1175/1520-0450\(1983\)022<1065:BPOTSF>2.0.CO;2](https://doi.org/10.1175/1520-0450(1983)022<1065:BPOTSF>2.0.CO;2)
- 469 Manobianco J (1989) Explosive east coast cyclogenesis over the west-central North Atlantic Ocean: A
470 composite study derived from ECMWF operational analyses. *Mon Wea Rev* 117(11):2365–2383.
471 [https://doi.org/10.1175/1520-0493\(1989\)1172.0.CO;2](https://doi.org/10.1175/1520-0493(1989)1172.0.CO;2)
- 472 Nakamura H (1993) Horizontal divergence associated with zonally isolated jet streams. *J Atmos Sci*
473 50(14):2310–2313. [https://doi.org/10.1175/1520-0469\(1993\)0502.0.CO;2](https://doi.org/10.1175/1520-0469(1993)0502.0.CO;2)
- 474 Petty G W, Miller D K (1995) Satellite microwave observations of precipitation correlated with
475 intensification rate in extratropical oceanic cyclones. *Mon Wea Rev* 123(6):1904–1911.
476 [https://doi.org/10.1175/1520-0493\(1995\)1232.0.CO;2](https://doi.org/10.1175/1520-0493(1995)1232.0.CO;2)
- 477 Reader M C, Moore G K (1995) Stratosphere-troposphere interactions associated with a case of explosive
478 cyclogenesis in the Labrador Sea. *Tellus* 47(5):849–863.
479 <https://doi.org/10.1034/j.1600-0870.1995.00124.x>
- 480 Rice R B (1979) Tracking a killer storm. *Sail* 10: 106–107.
- 481 Roebber P J (1984) Statistical analysis and updated climatology of explosive cyclones. *Mon Wea Rev*
482 112(8):1577–1589. [https://doi.org/10.1175/1520-0493\(1984\)1122.0.CO;2](https://doi.org/10.1175/1520-0493(1984)1122.0.CO;2)
- 483 Sanders F (1986) Explosive cyclogenesis in the west-central North Atlantic Ocean, 1981–84. Part I:
484 Composite structure and mean behavior. *Mon Wea Rev* 114(10):1781–1794.
485 [https://doi.org/10.1175/1520-0493\(1986\)1142.0.CO;2](https://doi.org/10.1175/1520-0493(1986)1142.0.CO;2)
- 486 Sanders F, Gyakum J R (1980) Synoptic-Dynamic Climatology of the “Bomb”. *Mon Wea Rev*
487 108(10):1589–1606 [https://doi.org/10.1175/1520-0493\(1980\)1082.0.CO;2](https://doi.org/10.1175/1520-0493(1980)1082.0.CO;2)
- 488 Schemm S, Wernli H (2014) The Linkage between the warm and the cold conveyor belts in an idealized
489 extratropical cyclone. *J Atmos Sci* 71(4):1443–1459. <https://doi.org/10.1175/JAS-D-13-0177.1>
- 490 Taguchi B, Nakamura H, Nonaka M, Xie S P (2009) Influences of the Kuroshio/Oyashio extensions on
491 air-sea heat exchanges and storm-track activity as revealed in regional atmospheric model simulations
492 for the 2003/04 cold season. *J Climate* 22(24):6536–6560. <https://doi.org/10.1175/2009JCLI2910.1>
- 493 Uccellini L W, Kocin P J (1987) The interaction of jet streak circulations during heavy snow events along the
494 east coast of United States. *Wea Forecasting* 2(4):289–308.
495 [https://doi.org/10.1175/1520-0434\(1987\)0022.0.CO;2](https://doi.org/10.1175/1520-0434(1987)0022.0.CO;2)
- 496 Wang C C, Rogers J C (2001) A composite study of explosive cyclogenesis in different sectors of the North
497 Atlantic. Part I: Cyclone structure and evolution. *Mon Wea Rev* 129(6):1481–1499.
498 [https://doi.org/10.1175/1520-0493\(2001\)1292.0.CO;2](https://doi.org/10.1175/1520-0493(2001)1292.0.CO;2)
- 499 Wash C H, Hale R A, Dobos P H, Wright E J (1992) Study of explosive and nonexplosive cyclogenesis
500 during FGGE. *Mon Wea Rev* 120(1):40–51. [https://doi.org/10.1175/1520-0493\(1992\)1202.0.CO;2](https://doi.org/10.1175/1520-0493(1992)1202.0.CO;2)
- 501 Wash C H, Peak J E, Calland W E, Cook W A (1988) Diagnostic study of explosive cyclogenesis during
502 FGGE. *Mon Wea Rev* 116(2):431–451. [https://doi.org/10.1175/1520-0493\(1988\)1162.0.CO;2](https://doi.org/10.1175/1520-0493(1988)1162.0.CO;2)

- 503 Yoshida A, Asuma Y (2004) Structures and environment of explosively developing extratropical cyclones in
504 the northwestern Pacific region. *Mon Wea Rev* 132(5):1121–1142.
505 [https://doi.org/10.1175/1520-0493\(2004\)1322.0.CO;2](https://doi.org/10.1175/1520-0493(2004)1322.0.CO;2)
- 506 Zhang S, Fu G, Lu C, Liu J W (2017) Characteristics of explosive cyclones over the Northern Pacific. *J Appl*
507 *Meteor Clim* 56(12):3187–3210. <https://doi.org/10.1175/JAMC-D-16-0330.1>
508

509

Table 1 Configuration for WRF model simulation

Model Setting and Option	Specification
Map projection	Lambert
Central point	35.0 °N, 130.0 °E
Domain	
Grid number	201×151
Horizontal resolution	20 km
Vertical grid	51 η^* with a pressure top at 50 hPa
Simulation duration	0000 UTC 23 Dec – 0000 UTC 25 Dec, 2017
Time step	120 s
PBL scheme	YSU scheme (Hong et al., 2006)
Cumulus parameterization	Kain-Fritsch scheme (Kain, 2004)
Microphysics	Thompson scheme (Thompson et al., 2008)
Long-shortwave radiation	RRTMG scheme (Iacono et al., 2008)
Land surface model	Noah land surface model (Tewari et al., 2004)

510

511

512

513

514

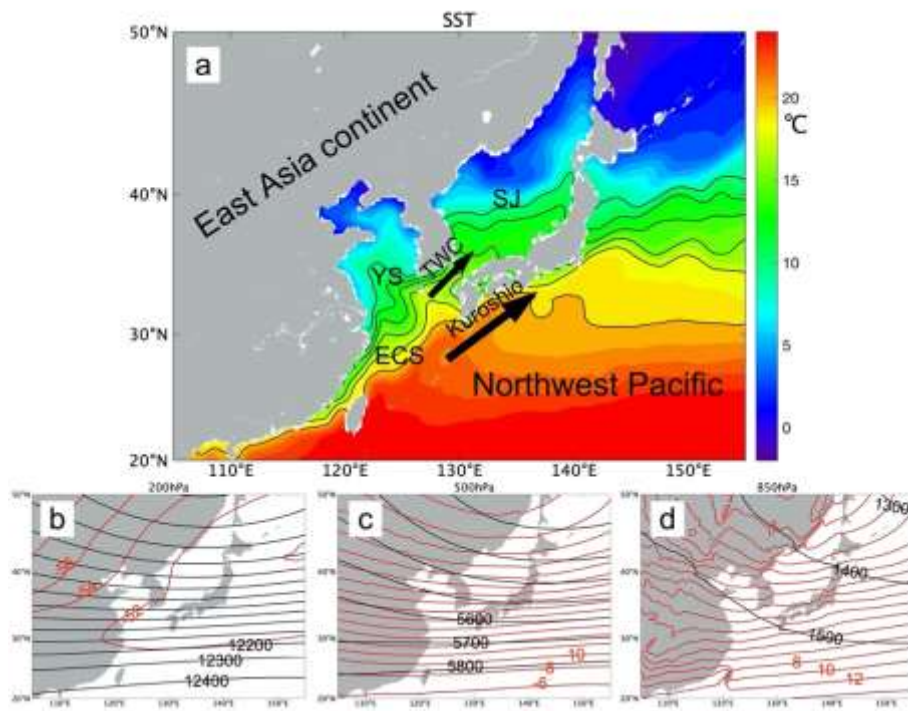
* η =1.00000, 0.99381, 0.98643, 0.97786, 0.96815, 0.95731, 0.94538, 0.93122, 0.91490, 0.89653, 0.87621, 0.85405, 0.82911, 0.80160, 0.77175, 0.73981, 0.70509, 0.66798, 0.62889, 0.58823, 0.54957, 0.51281, 0.47788, 0.44471, 0.41323, 0.38336, 0.35503, 0.32819, 0.30276, 0.27869, 0.25592, 0.23439, 0.21405, 0.19484, 0.17672, 0.15963, 0.14352, 0.12836, 0.11410, 0.10070, 0.08811, 0.07630, 0.06523, 0.05487, 0.04517, 0.03611, 0.02765, 0.01977, 0.01243, 0.00560, 0.00000

515 **Table 2** Summary of sensitivity experiments

Experiment	Specification
Exp-MH	Global relative humidity is cut in half
Exp-SST	Global SST is decreased by 4 °C
Exp-MT	Air temperature is increased in the northwest part of initial and boundary conditions
Exp-MT+MH	Air temperature is modified as Exp-MT, while relative humidity is modified as Exp-MH

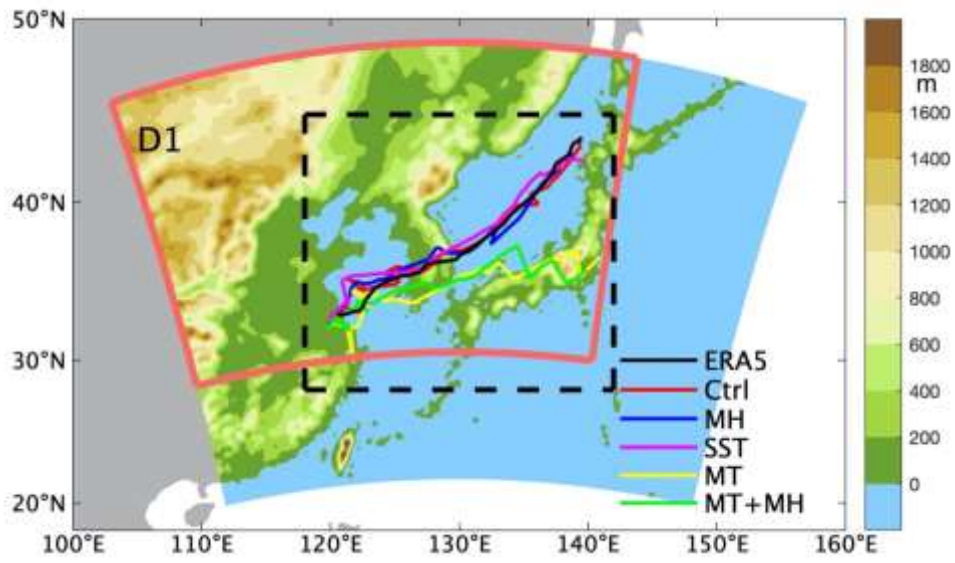
516

517



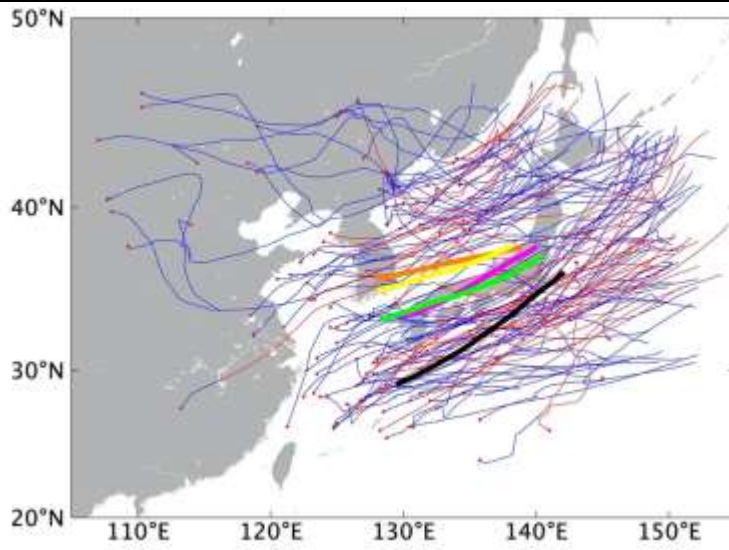
518
519
520
521
522

Fig. 1 SST (a) and synoptic features at 200 hPa (b), 500 hPa (c) and 850 hPa (d) averaged in winters during 2010–2019. Contours in (a) show the SST within 10–20 °C with an interval of 2 °C. “YS”, “ECS”, “SJ” and “TWC” denote the Yellow Sea, East China Sea, Sea of Japan and Tsushima Warm Current, respectively. Black and red contours in (b–d) represent GPH (gpm) and air temperature (°C)



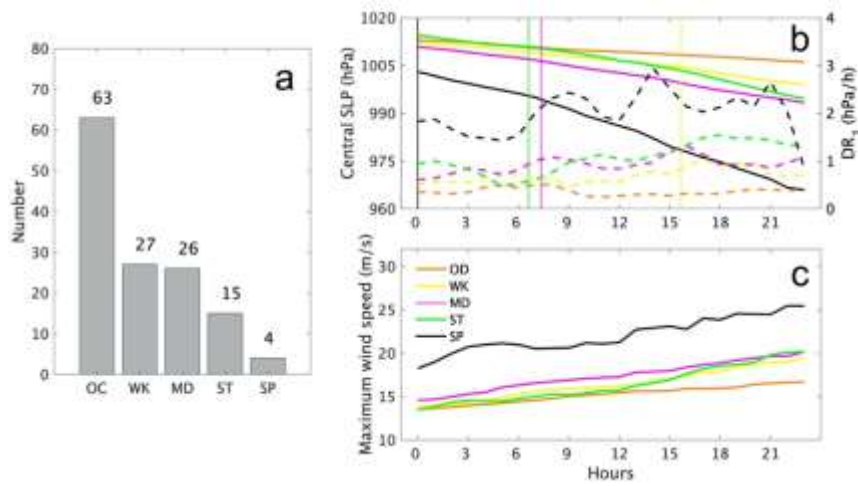
523
524
525
526
527
528

Fig. 2 Model domain for WRF simulation. Shadings denote the terrain (m) within model domain. Dashed frame denotes the domain where PV tendency is calculated in average. Thick pink frame locates where the temperature is modified for Exp-MT and Exp-MT+MH. Other lines show the cyclone tracks within 1200 UTC 23 Dec – 0000 UTC 25 Dec, 2017 retrieved from reanalysis and simulation experiments



529
530
531
532
533

Fig. 3 Cyclone tracks over the East Asia in 10 winters. Thin lines denote tracks for the 135 cyclones. Red parts denote where cyclones were explosively deepened. Red dots denote the initial locations. Thick orange, yellow, purple, green and black lines denote the average 24-h tracks for OCs, weak, medium, strong and super ECs



534

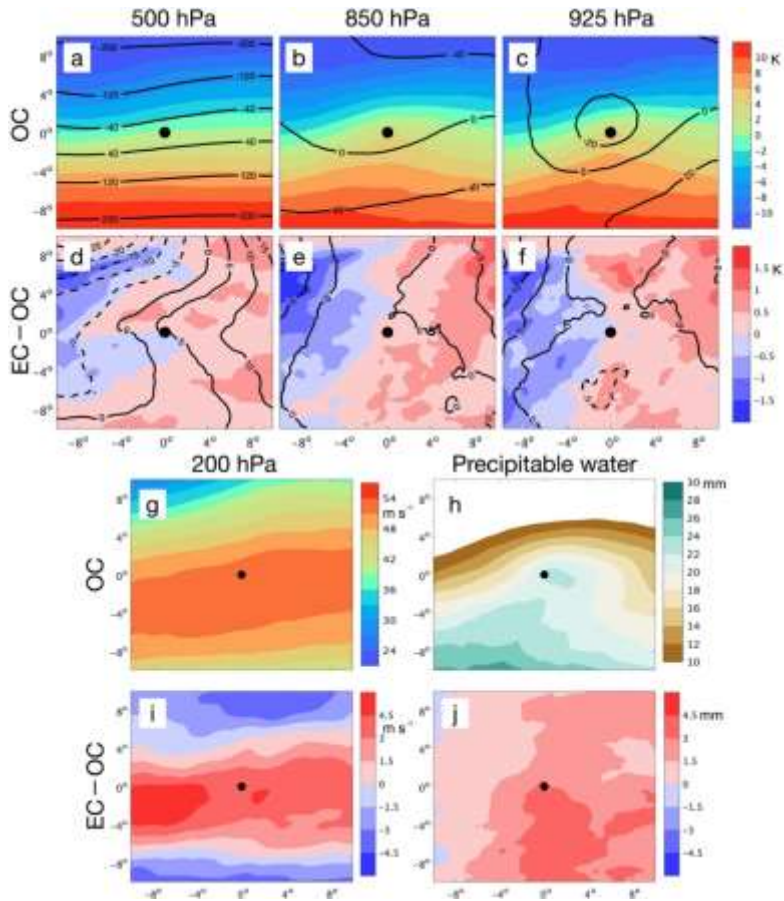
535

536

537

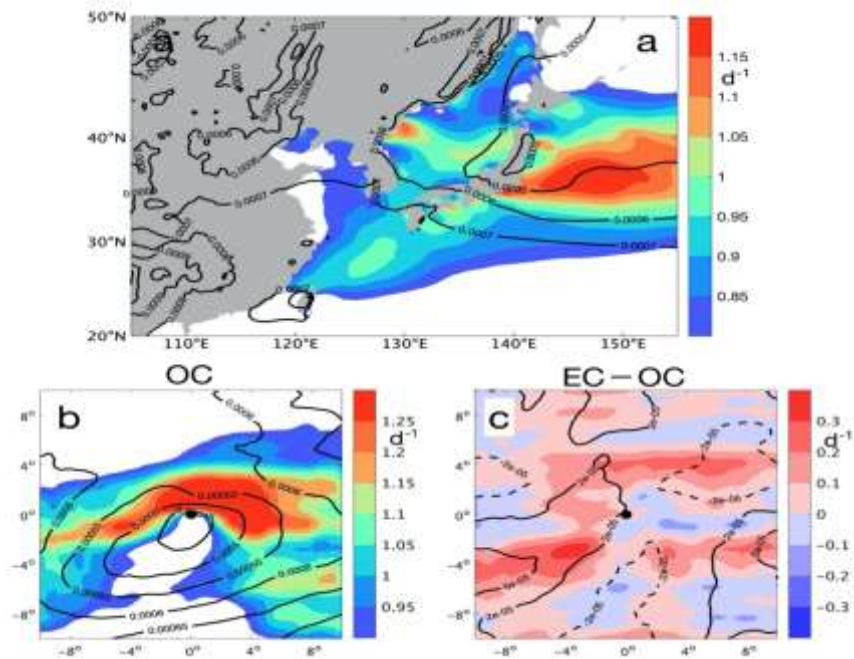
538

Fig. 4 Numbers of different ranks of cyclones (a), 24-h variation of their central SLPs (b) and max wind speed (c). Solid and dashed curves in (b) represent the central SLPs and 1-h deepening rate, respectively, and vertical lines show the beginning of explosive growth. “WK”, “MD”, “ST” and “SP” denote weak, medium, strong and super ECs, respectively



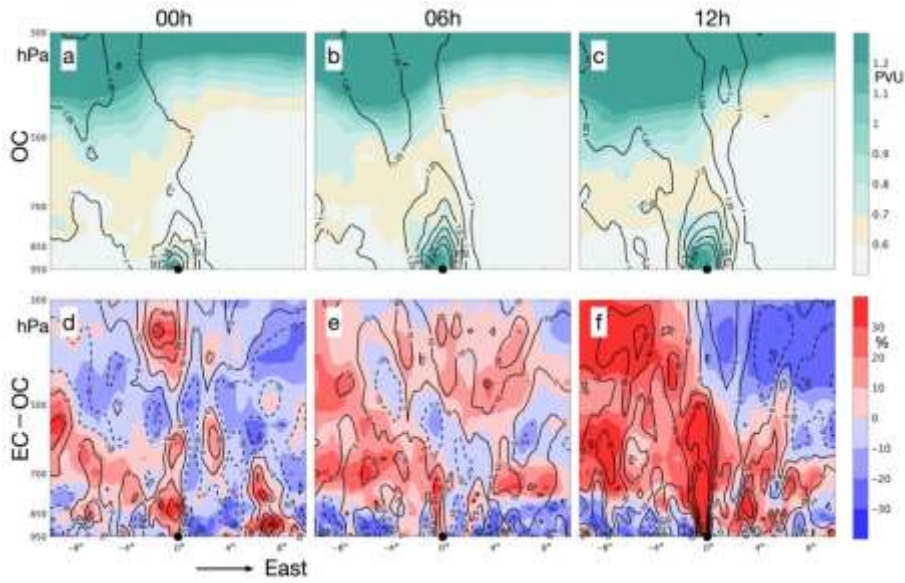
539
 540
 541
 542
 543
 544
 545

Fig. 5 Comparison of initial conditions for OCs and ECs. 1st row shows average potential temperature anomaly (shadings) and GPH anomaly (gpm; contours) for OCs at 500 (a), 850 (b) and 925 (c) hPa. 2nd row shows the difference of average potential temperature anomaly (shadings) and GPH anomaly (gpm; contours) between ECs and OCs at 500 (d), 850 (e) and 925 (f) hPa. 3rd row shows average 200 hPa wind speed (g) and precipitable water (h) for OCs. 4th row shows the difference of average 200 hPa wind speed (i) and precipitable water (j) between ECs and OCs.



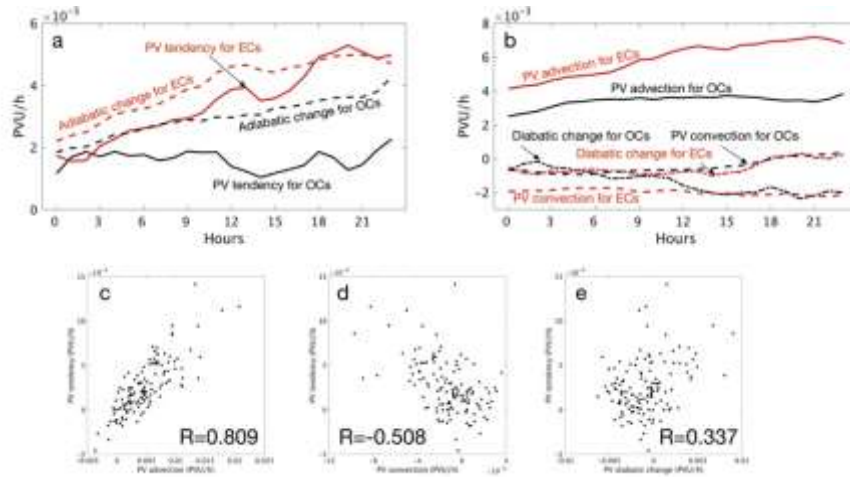
546
 547
 548
 549
 550
 551
 552
 553

Fig. 6 Low-level baroclinicity and static stability over East Asia (a) and around OC center (b), and the difference between ECs and OCs (c). Shadings denote E_g , and contours denote Γ (unit: K Pa^{-1}). Solid/dashed lines in (c) denote average Γ for ECs larger/smaller than OCs. Both variables are retrieved from “daily values” between 850 and 700 hPa. For (a), “daily values” are the potential temperatures and wind velocities averaged during 00–23 UTC of each day, and E_g and Γ are averaged within 10 winters. For (b–c), “daily values” are averaged in relative geographic coordinates within the $20^\circ \times 20^\circ$ square domain around the center during the first 24 h for each cyclone, and E_g and Γ are averaged among all OCs or ECs.



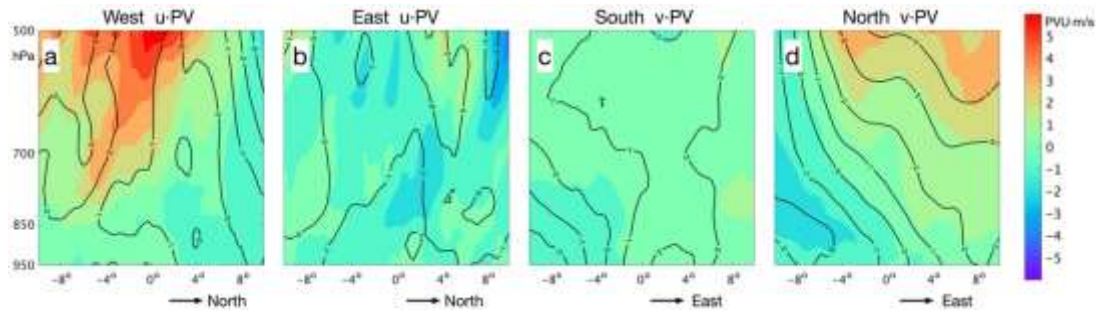
554
 555
 556
 557
 558
 559

Fig. 7 Zonal cross sections of average PV and relative vorticity going through the cyclone center during initial development. 1st row shows the average PV (shadings) and relative vorticity (contours; unit: 10^{-4} s^{-1}) for OCs. 2nd row shows the difference of PV (shadings) and relative vorticity (contours; unit: %) between ECs and OCs, with solid/dashed lines denoting relative vorticity for ECs larger/smaller than OCs. Left/middle/right column shows the situation 0/6/12 h after the cyclones are identified



560
 561
 562
 563
 564

Fig. 8 Contribution of PV advection, vertical transport and diabatic change to PV tendency. 1st row shows the variation of each term during initial development averaged among OCs (black lines) and ECs (red lines). 2nd row shows the distribution of PV tendency and PV advection (a)/vertical transport (b)/diabatic change (c) averaged during the 24 h for each cyclone, with R denoting the correlation coefficient.



565

566

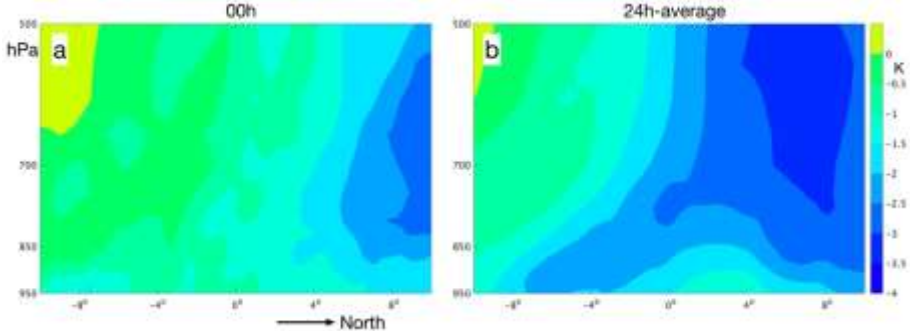
567

568

569

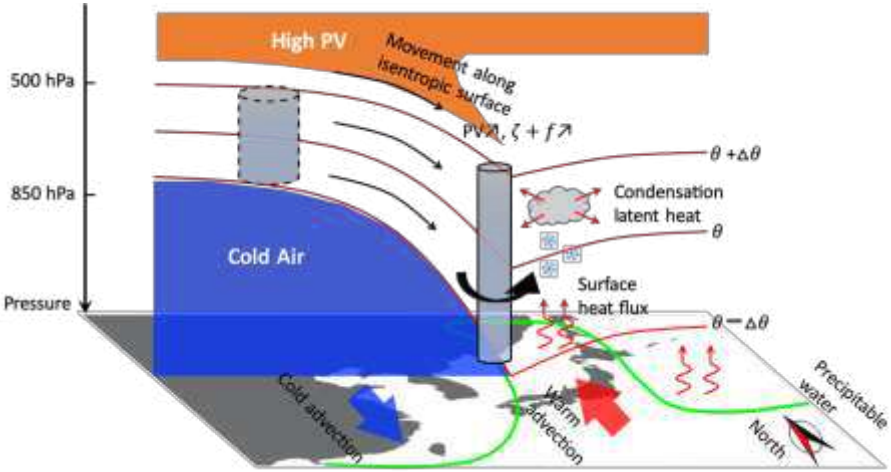
570

Fig. 9 Difference of wind speed and components of PV advection between ECs and OCs at the west (a), east (b), south (c) and north (d) boundary. For the west (a) and east (b) boundary, contours denote zonal wind speed and shadings denote product of zonal wind speed and PV. For the south (c) and north (d) boundary, contours denote meridional wind speed and shadings denote product of meridional wind speed and PV. All variables are averaged during the 24 h

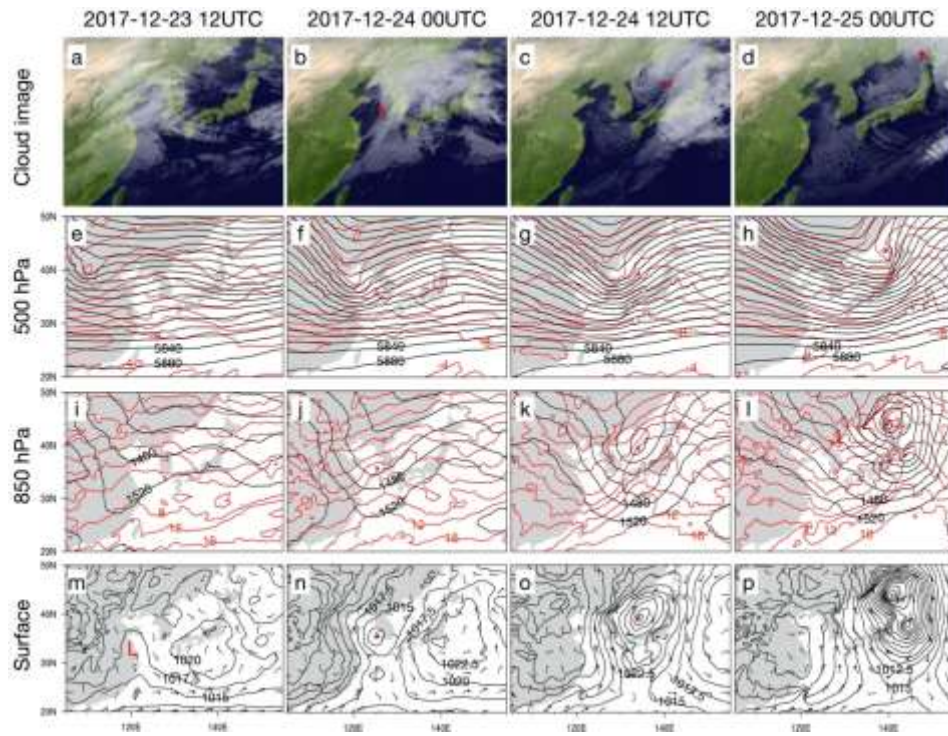


571
572
573
574

Fig. 10 Difference of potential temperature anomaly between ECs and OCs at the west boundary at initial time (a) and averaged during the 24 h (b)

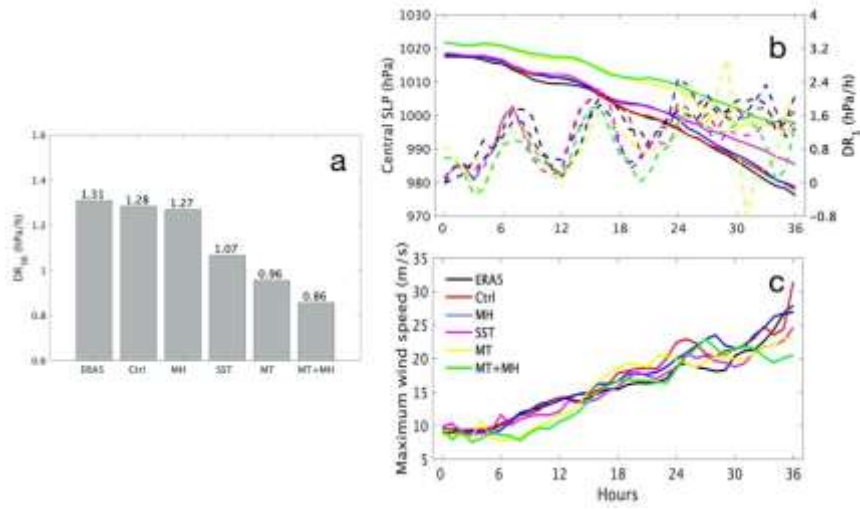


575
576 **Fig. 11** Schematic diagram of multi-factors that impact the development of a cyclone
577



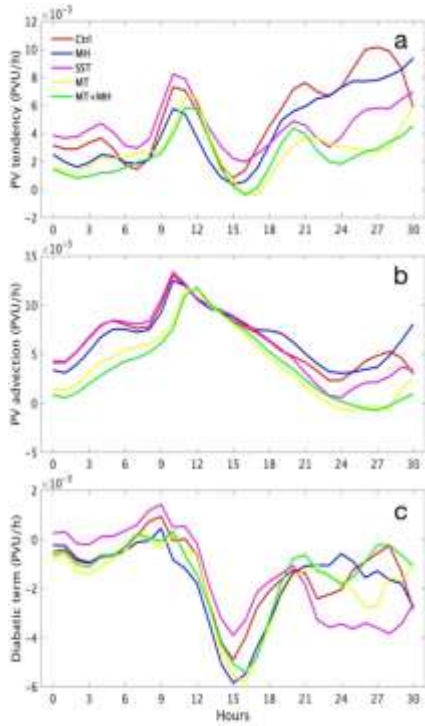
578
579
580
581
582

Fig. 12 Infrared cloud images and synoptic situations during 23–24 Dec 2017. 1st row shows the cloud images. 2nd row shows GPH (gpm; black contours) and temperature (°C; red contours) at 500 hPa. 3rd row is the same as 2nd row, except at 850 hPa. 4th row shows the SLP (hPa; black contours) and surface wind (wind barbs). Each column shows situation at the time marked top



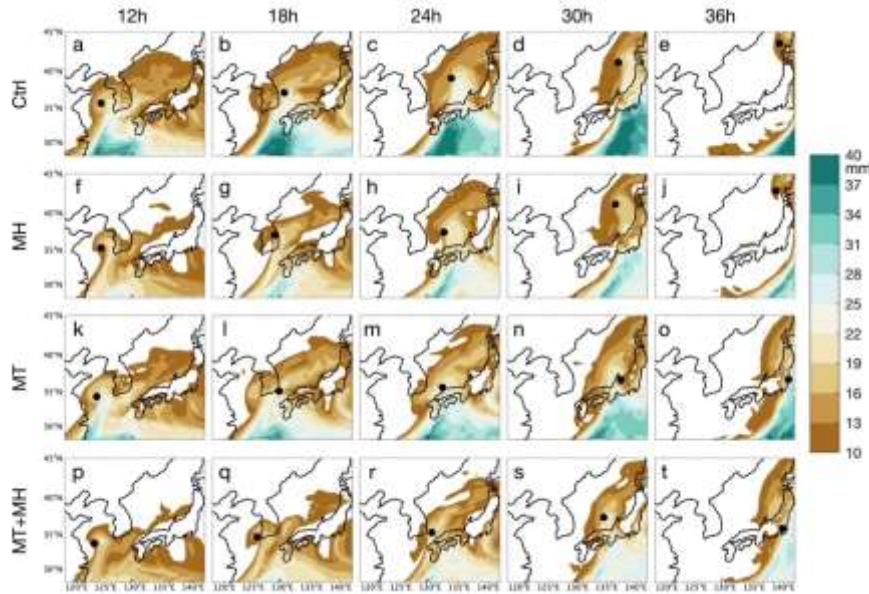
583
584
585
586
587

Fig. 13 36-h deepening rates (a), variation of cyclone central SLPs (b) and maximum wind speeds (c) for reanalysis and 5 experiments during 1200 UTC 23 Dec – 0000 UTC 25 Dec. Solid and dashed curves in (b) represent the central SLPs and 1-h deepening rate, respectively



588
589
590
591

Fig. 14 Variation of local PV tendency (a), PV advection (b) and diabatic term (c) for each simulation experiment during 1200 UTC 23 Dec – 1800 UTC 24 Dec. Each term is averaged within 500–950 hPa over the dashed frame in Figure 2



592
593
594
595
596

Fig. 15 Precipitable water around cyclone center for each simulation experiment. 1st/2nd/3rd/4th row shows the precipitable water for Exp-Ctrl/Exp-MH/Exp-MT/Exp-MT+MH. Each column shows situation at the time marked top